On the geometry of demixing: A study of lipid phase separation on curved surfaces

Rinaldin, M.

CHAPTER 3

LIPID DEMIXING ON COLLOIDS

3

Unravelling the physical mechanisms behind the organisation of lipid domains is a central goal in cell biology and membrane biophysics. Previous studies on model lipid bilayers featuring phase-separated domains found an intricate interplay between the membrane geometry and its chemical composition. However, the lack of a model system with simultaneous control over the membrane shape and conservation of its composition precluded a fundamental understanding of curvature-induced effects. Here we introduce a new class of multicomponent vesicles supported by colloidal scaffolds of designed shape. Thanks to a combination of experiments, theoretical modelling and numerical simulations, we demonstrate that the local substrate geometry and global chemical composition of the bilayer determine both the spatial arrangement of the domains and the sorting of the lipids. Strong geometric anisotropy, in particular, drives the occurrence of a new state, in which the lipids are inhomogeneously mixed in a curvature-dependent fashion. Our results provide critical insights into the phase separation of lipid membranes and curved surfaces in general.

This chapter is the result of a collaboration with Piermarco Fonda who developed and performed the analytical calculations and numerical simulations presented here. The text is based on:

M. Rinaldin*, P. Fonda*, L. Giomi, and D. J. Kraft, Geometric pinning and antimixing in scaffolded lipid vesicles, *arXiv:1804.08596* (2018).

* The authors contributed equally to the work.

3.1 Introduction

In eukaryotic cells, membranes possess specialised lipid domains that differ in their lipid and protein composition. The organisation of these domains is responsible for many cellular functions, including trafficking and compartmentalisation[128]. Generation and maintenance of these domains is often associated with curvature, *e.g.* negative membrane curvature is linked to clustering of conical lipids by bacterial toxins[129], and budded domains can sort receptors as trafficking carriers[130] .

The correlation between membrane geometry and chemical composition has also been observed extensively in model lipid membranes consisting of ternary mixtures of phospholipids and cholesterol. While chemically homogeneous at high temperatures, below a specific temperature they spontaneously separate into two liquid phases. These phases, known as liquid-ordered (LO) and liquid-disordered (LD), differ by lipid composition and material properties, such as bilayer thickness and bending resistance[6;65;66]. Specifically, the LD phase is thinner and softer and therefore it is preferentially localised on the more curved regions. Experiments on giant unilamellar vesicles (GUVs)[4;7;12;17;65;131 5;18] reported a twofold correlation between these lipid domains and membrane geometry. While local membrane curvature can favour lipid segregation and domain nucleation and localisation, the presence of lipid domains can also drive the formation of curved regions, including buds, necks, and protrusions[4]. To solve this causality dilemma, several experimental setups have been proposed to control membrane shape and investigate its effect on phase separation patterns. One method for setting the geometry of the membrane consists of pulling highly curved tubes from GUVs. These experiments showed that close to the demixing point the more curved the tubes are, the higher is the number of unsaturated lipids partitioning in the tubes, therefore demonstrating that curvature affects lipid sorting[6–8]. Other systems consist of creating lipid bilayers on substrates with curved geometry. This has been performed by approaching GUVs to curved surfaces[18;19] and using supported lipid bilayers on patterned surfaces[5]. In both these experimental systems, disordered domains preferentially position in the regions of higher curvature.

While these experiments have contributed significantly to our understanding of the physics and chemistry of liquid-liquid phase separation in membranes, they could not disentangle the correlation between membrane geometry, lipid composition, and resulting phase separation patterns. In GUVs, the membrane shape can change during the phase separation process. In SLBs, while membrane geometry can be prescribed, the large overall size and presence of boundaries in the substrates hinders the understanding of the effect of the lipid composition on the phase separation patterns[5;18].

In this way, a biophysical mechanistic understanding of curvature-related effects in phase-separated lipid membranes remains still incomplete. In this work, we overcome these limitations by using colloid supported lipid bilayers (CSLBs) which are supported lipid bilayers on colloidal particles and were introduced in Chapter 2. By tuning the shape of the colloids, we obtain different shapes for the membrane. Importantly, colloidal particles, differently from patterned surfaces, have a closed surface, *i.e.* a surface that is compact and does not have boundaries. By imposing a close and prescribed surface to the membrane, we show here that we can determine the relation between membrane

shape and phase separation patterns. Moreover, these features also allow us to discover a generalisation of curvature-induced lipid sorting observed in GUVs[6–8].

3.2 Methods

3.2.1 Reagents. The lipids 1-palmitoyl-2-oleoyl-*sn*-glycero-3-phosphocholine (POPC), porcine brain sphingomyelin (BSM), ovine wool cholesterol (chol), 1,2-dioleoyl-*sn*-glycero-3-phosphoethanolamine-N-[methoxy(polyethylene glycol)-2000] (DOPE-PEG (2000)), and L-α-Phosphatidylethanolamine-N-(DOPE lissamine rhodamine B sulfonyl) were purchased from Avanti Polar Lipids and stored at $-20\,^{\circ}\mathrm{C}$. HEPES buffer was made with 115 mM NaCl, 1.2 mM $CaCl_2$, 1.2 mM $MgCl_2$, 2.4 mM K_2HPO_4 and 20 mM HEPES, all purchased from Sigma Aldrich. Ethanol puriss. $\geq$ 99.8% and ammonia solution (NH_4OH) 28%-30% were obtained from Honeywell. Sodium hydroxide (NaOH) pellets $\geq$ 97%, iron (III) chloride (FeCl3) hexahydrate puriss. 98-100%, tetraethyl orthosilicate acid (TEOS) 37%, hydrochloric acid (HCl) 37%, potassium chloride (KCl) 99+% , and tetramethylammonium hydroxide solution (TMAH, 25% wt) were purchased from Sigma Aldrich. All chemicals were used as delivered. All solutions were prepared with Milli-Q water.

3.2.2 Colloidal particles. Commercial silica spheres of size $(2.06 \pm 0.05)\,\mu\mathrm{m}$ were synthesised by Microparticles GmbH, using a Stöber method where tetraethoxysilane (TEOS) reacts with water and bases in an ethanolic solution (sol-gel process).

Hematite colloids with a cubic shape were synthesised following the sol-gel method of Sugimoto *et al.*[41]. Specifically, a sodium hydroxide (NaOH) solution was prepared by dissolving 20.14 g of NaOH in 100 mL of MilliQ water. This solution was added in 50 s to a 100 mL solution of 50.39 g iron (III) chloride ($FeCl_3$) dissolved in water while magnetically stirring at 300 rpm. Weighting of the $FeCl_3$ was done quickly because the salt is very hygroscopic. The mixture was stirred for another 10 minutes at 450 rpm and then transferred to a preheated oven at 100 °C, where it was left undisturbed for 10 days. The resulting cubic particles have a superball shape which can be described by the parameter m[132]:

$$m = \frac{\log 2}{0.5 \log 2 - \log \frac{L}{D}}, \tag{3.1}$$

where L and D are respectively the side and the corner-to-corner length of the cubic particle. The hematite cubes obtained from our synthesis had a $m-$value of 3.3 ± 0.6 and a corner-to-corner distance of $(1.76 \pm 0.08)\,\mu\mathrm{m}$. A transmission electron microscopy (TEM) image of the particles is shown in Figure 3.1a. The particles were washed and stored in ethanol. To coat the particles with a silica layer, we followed a method described by Rossi *et al.*[37]. The reaction was preformed at 15 - 20 °C in a 2L round bottom flask positioned in an ultrasonic bath (Elmasonic P300H, Elma). The reaction flask contained a uniform mixture of 920 mL ethanol, 62 mL of water, 42 mL of cube dispersion (3.8 %wt), and 10 mL of TMAH dissolved in water (1% wt). A mixture of 15 mL of TEOS and 15 ml ethanol was added to the reaction flask at a rate of 230 µL/min using a syringe pump (Harvard apparatus). After addition, the reaction mixture was sonicated for 3h and

mechanically stirred for another 16h to ensure that all TEOS had reacted (Figure 3.1b). These silica coated hematite cubes were then turned into hollow silica cubes by dissolving the hematite cores in 5M hydrochloric acid. The hollow silica cubes were washed three times and stored in ethanol (Figure 3.1c). Since the silica coating was performed without polymers to allow for bilayer functionalisation (see Chapter 2), large aggregates were obtained. To remove the aggregates from the single particles, cycles of centrifugation was applied and particles were used within a week from the synthesis.

Colloidal symmetric and asymmetric dumbbell-shaped particles consisting of polystyrene (PS) and 3-(Trimethoxysilyl)propyl methacrylate (TPM) were synthesised using a modified version of the procedure described by Kim J. *et. al.*[133]. Linear polystyrene particles were synthesised by a dispersion polymerisation method and cross-linked by the addition of a swelling solution containing styrene and TPM in 90:10 ratio and divinylbenzene (DVB). After polymerisation was initiated by azobisisobutyronitrile (AIBN), a second swelling step was performed to create a protrusion on the cross-linked spheres. Depending on the swelling ratio S, which is defined as the mass of the monomer divided by the mass of the polymer colloids, dumbbell particles ($S = 3$) or asymmetric dumbbell shapes ($S = 4$) were obtained. The symmetric dumbbell-shaped particles have a total length of (5.23 ± 0.05) µm, the ratio between the diameters of the two lobes equals 0.98 $\pm$ 0.04, and the smaller lobe diameter equals (2.68 ± 0.04) µm. (Figure 3.1d). The asymmetric dumbbell-shaped particles have a total length of (4.01 ± 0.04) µm, the ratio between the diameters of the two lobes equals 0.57 ± 0.02, and the smaller lobe diameter equals (1.45 ± 0.03) µm. (Figure 3.1e). To achieve adsorption of the lipids to the surface of these particles, the dumbbell-shaped particles were coated with silica. We used a modified version of the protocol by Wang *et al.* to coat hematite particles[134]. Typically, 0.5 mL TEOS was added to an ultrasonicated mixture of 100 mL ethanol, 15 mL ammonia (28%-30%) and 5 mL of particle dispersion (0.5% wt), while mechanically stirring for 5h. The silica coated colloids were washed and stored in ethanol.

To investigate how different silica surfaces affect the phase separation of the bilayer, we prepared silica particles with a dumbbell shape and with a size comparable to the silica-coated PS-TPM particles through an alternative route. Colloidal symmetric and asymmetric dumbbell-shaped particles of silica were obtained by destabilisation of charge-stabilised silica spheres. Destabilisation was achieved by mixing a solution of 200 µL potassium chloride (KCl) with 100 µL dispersion of silica particles in water (5 % wt). The mixture was tumbled end-over-end for 20 minutes before being quenched with 20 mL water. The resulting aggregates consisted of varying numbers of spheres and were washed six times with water to remove KCl and re-stabilise the particles. We coated an aliquot of the dispersion with a lipid bilayer and then only inspected phase separation on aggregates consisting of two spheres. In the Appendix "Surface properties analysis" and Figure A.2, we report that the type of silica surface of the colloids does not affect our results.

3.2.3 Lipid bilayer coating. A mixture of 500 µg of SM, POPC, and cholesterol in 2:1:1 mole ratio was prepared in chloroform. This mole ratio was chosen because it allows for liquid-liquid phase separation in GUVs and CSLBs, see Figure A.1 in the Appendix and Petruzielo *et al.*[135]. 0.2% mole fraction of Liss Rhod PE and C11 TopFluor SM were

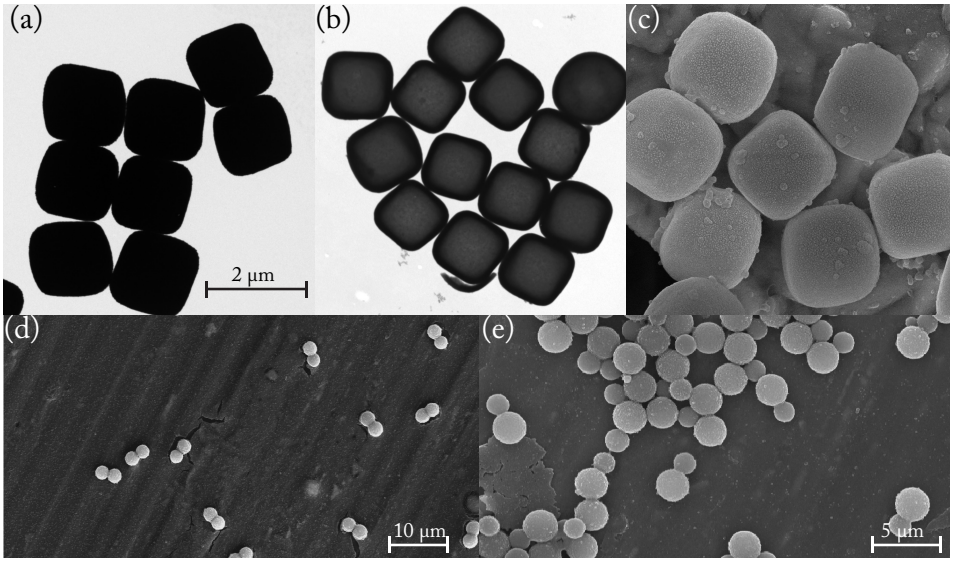

Figure 3.1: Electron microscopy images of colloidal particles. **(a)** Transmission electron microscopy (TEM) image of hematite cubes, **(b)** TEM image of silica coated hematite cubes, and **(c)** scanning electron microscopy (SEM) image of silica cubes after dissolution of the hematite core. **(d)** SEM image of PS-TPM symmetric dumbbell-shaped particles. **(e)** SEM image of PS-TPM asymmetric dumbbell-shaped particles.

added to fluorescently label the LD and LO phases, respectively. 5% mole fraction of the PEGylated lipid DOPE-PEG(2000) was added to improve the mobility of the bilayer. The lipids were dried by vacuum desiccation for two hours and then re-suspended to a 2 mg/mL solution with HEPES buffer. The solution was vortexed for 15 minutes and heated to 70 °C. The lipid solution was extruded 21 times with a mini extruder (Avanti Polar Lipids) equipped with two 250 μL gas-tight syringes (Hamilton), four drain discs, and one nucleopore track-etch membrane with 0.03 μm pores diameter (Whatman). To keep the lipids above transition temperature, the extruder was placed on a heating plate set at 70°C. Then, in a rotavapor (Buchi) 50 μL of SUVs were added to 1 mL of 0.05 %w/v of particles dispersed in HEPES. Particles were left undergoing gentle rotation at 70°C for one hour. The solution was then centrifuged at 3000 rpm for 10 minutes and the supernatant was replaced with HEPES to remove SUVs in excess.

3.2.4 Imaging and analysis. The CSLBs were imaged at room temperature with an inverted confocal microscope (Nikon Eclipse Ti-E) equipped with a Nikon A1R confocal scanhead with galvano and resonant scanning mirrors. A 100x oil immersion objective (NA=1.4) was used. 488 and 561 nm lasers were used to excite the C11 TopFluor SM and Rhodamine dyes, respectively. Lasers passed through a quarter-wave plate to avoid

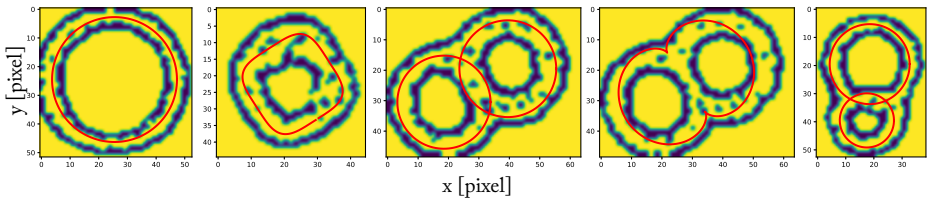

Figure 3.2: Equatorial sections of CSLBs. From left to right: sphere, cube, symmetric, and asymmetric dumbbell-shaped particles after Gaussian threshold and blur. The images are fitted with a circle, a squircle, a nephroid, and two circles indicated by the red lines, respectively.

the polarisation of the dyes and the emitted light was separated by using 500-550 nm and 565-625 nm filters.

3.2.5 Analysis of phase-separated configurations. Three-dimensional image stacks were acquired by scanning the sample in the z direction with a MCL Nano-drive stage and reconstructed with Nikon AR software. We calculated the percentage of area occupied by the LD and LO phases by analysing the fluorescent signal of the DOPE-Rhodamine and the C11 TopFluor SM, respectively. For each slice of the zeta-stack we applied a threshold to both channels to eliminate random noise and correct, at least partially, the crosstalk between the two dyes. Then, we applied a Gaussian threshold and blur to enhance the edges of the membrane. Finally, we fitted with 1000 points the intensity profile of the spheres, cubes, symmetric and asymmetric dumbbell-shaped particles to a circle, a squircle, a nephroid, and two circles, respectively (Figure 3.2). For the dumbbell-shaped particles, we compared the quality of the fits by two circles and by a nephroid and chose the shape with the best fit. From the fit, we retrieved the values of the intensity in the magenta and green channels and normalised them with the value of the maximum intensities. We checked along the points of the profile which normalised intensity was higher and:

- if $I_m > I_g$, we defined that point to belong to the LD phase,
- if $I_g > I_m$, we defined that point to belong to the LO phase,

where I_m, I_g are the intensities relative to the magenta and green channels, respectively. Then, we averaged the results over all points of the slice. We found the total percentage of area occupied by one phase of the image stack by calculating the mean of the line fractions in all slices. The scripts used for the analysis can be found on Github[136].

3.2.6 Fluorescence recovery after photobleaching. As we have stressed in Chapter 2, a fundamental property of the lipid bilayer that allows for studying phase separation is its fluidity, which is the lateral diffusion of the lipids. To check the fluidity of the bilayer we used the fluorescence recovery after photobleaching (FRAP) technique. FRAP is a method consisting of bleaching a fluorescent area of the sample and observing the fluorescence recovery. In this work, we used FRAP to test the mobility of the bilayer

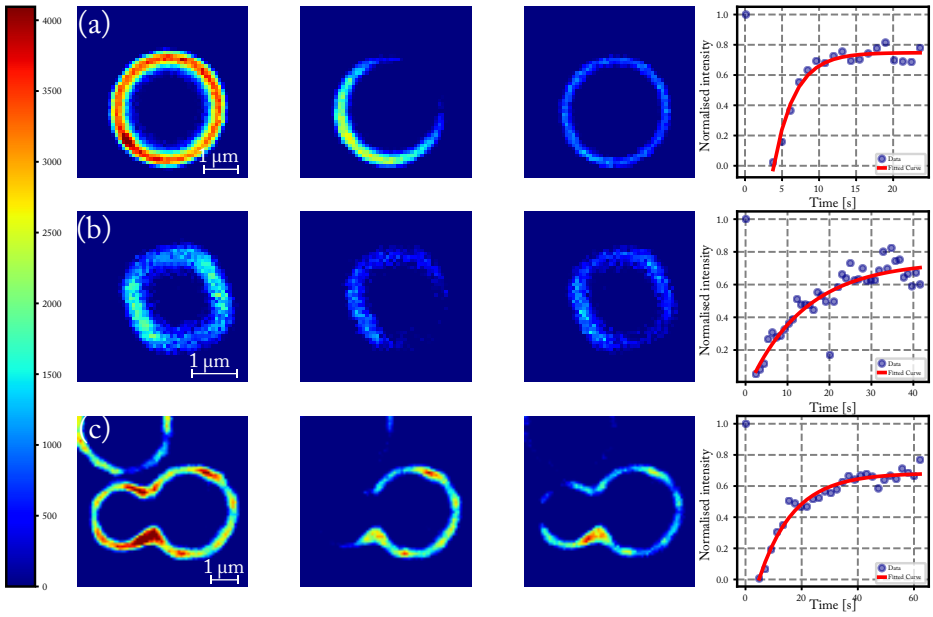

Figure 3.3: FRAP analysis of CSLBs. **(a)** Spherical, **(b)** cubic, and **(c)** asymmetric dumbbell-shaped CSLBs. From left to right: confocal microscopy images were taken before, directly after bleaching and after the recovery of the fluorescent signal. Full recovery cannot be obtained because the surface is closed. Images were taken at **(a)** t=0, 4, and 25 s; **(b)** t=0, 2, and 42 s; **(c)** t=0, 5, and 62 s. The fluorescent intensity is colour-coded as shown in the bar on the left. The column pn the right shows the respective data of the normalised intensity and the exponential fit.

in the following way: a circular area of the membrane containing fluorescent DOPE-Rhodamine lipids was bleached and the subsequent recovery of the intensity of this region was measured. We observed that the recovery of the signal is exponential (see Figure 3.3) and therefore fitted the data using the following function:

$$I_{\text{norm}}(t) = A\left(1 - e^{-\frac{t-t_0}{\tau}}\right) , \tag{3.2}$$

where $I_{\text{norm}}(t) = I(t)/[I(t=0)I(t)_{\text{ref}}]$ is the measured intensity $I(t)$ normalised with respect to the intensity just before bleaching $I(t=0)$ and corrected for bleaching through measurement of the intensity of a non-bleached reference area, $I(t)_{ref}$. A is the extent of the recovery, $t-t_0$ is the time elapsed since the beginning of the recovery process, and τ is the recovery time. We report in the following table the values of the parameters obtained from the fit in Figure 3.3.

Shape	**A**	$\mathbf{1/\tau\ [s^{-1}]}$	$\mathbf{t_0[s]}$
Sphere	0.75 ± 0.02	0.35 ± 0.04	3.9 ± 0.2
Cube	0.74 ± 0.05	0.07 ± 0.02	1 ± 1
Asymmetric dumbbell	0.68 ± 0.02	0.08 ± 0.01	4.8 ± 0.6

Table 3.1: Values of the parameters of the exponential fits shown in Figure 3.3.

3.3 Results and discussion

3.3.1 Multicomponent CSLBs. We fabricated multicomponent CSLBs by deposition of small unilamellar vesicles (SUVs) on colloidal particles (see schematics in Figure 3.4). SUVs were prepared from a ternary mixture of the lipids BSM, POPC, and cholesterol in a 2:1:1 mole ratio [135], and deposited on micrometer-sized particles of four shapes: spheres, cubes, and symmetric and asymmetric dumbbells. Even though one specific mole ratio of lipids was used in the experiments, the composition of single SUVs was randomly distributed around 2:1:1. This implies that a single deposition produces several CSLBs, each with different lipid composition, allowing us to simultaneously study multiple lipid concentrations for a given geometry.

Van der Waals and electrostatic forces attract the SUVs to the colloidal surfaces, which, due to their ampiphilic nature, fuse to form a closed lipid bilayer which envelopes the surface fully with nanometer precision [29]. To enhance this effect while preserving fluidity, we used colloids with a silica surface and 5% mole of the PEGylated lipid DOPE-PEG(2000) (top-right inset of Figure 3.4). We tested the fluidity of the membrane *via* fluorescence after photobleaching (FRAP) experiments.

After lipid deposition, we cooled the sample from 70 °C to room temperature to induce phase separation and imaged the membranes by using confocal fluorescence microscopy. We identified the LO (SM rich) and LD (POPC rich) phases through fluorescent labelling with C11 TopFluor SM and DOPE-Rhodamine [137] shown in green and magenta in Figure 3.4, respectively. We emphasise that all membrane components are present in both phases, albeit at different concentrations [137–141]. We exclude chemical composition changes due to oxidation by preparing the SUVs *via* extrusion rather than sonication and by keeping the sample in the dark. In this way, we also prevented bleaching.

3.3.2 The experimental diagram. Our multicomponent CSLBs enable us to study lipid phase separation of closed prescribed surfaces. While the global mole ratio of the three lipids of the SUVs is fixed at 2:1:1 of SM:POPC:chol, our set-up leads to the deposition of a random amount of lipids of each kind on any given CSLB, allowing for sampling multiple membrane compositions in a single experiment.

We assess whether a given CSLB is phase-separated or mixed by measuring the intensity of the two dyes at different locations on the surface. If the intensity signals from both dyes normalised with the maximum intensities overlap completely, the CSLB is in the mixed state, otherwise it is phase-separated. For phase-separated CSLBs, intensity profiles were acquired for 3D stacks of spherical- and dumbbell-shaped CSLBs using

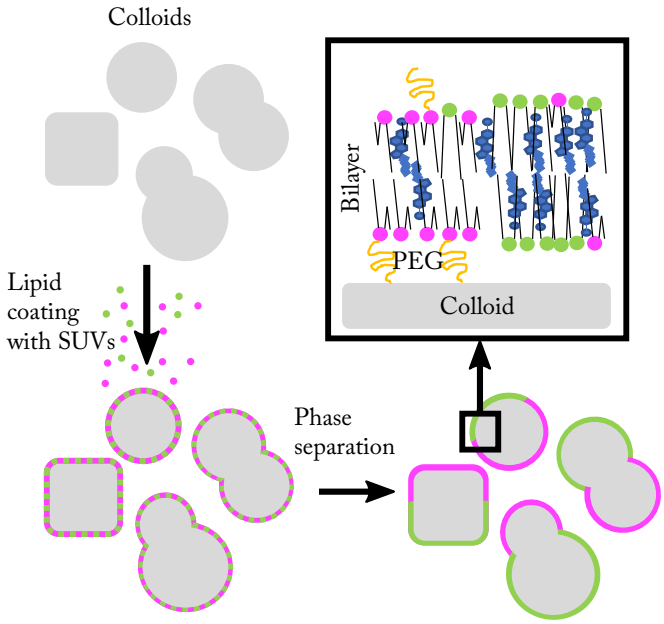

Figure 3.4: Schematic overview of the experimental system. Lipid coating of colloidal particles of spherical, cubic, symmetric and asymmetric dumbbell shape. After the temperature is lowered, the lipid bilayer undergoes phase separation. Liquid disordered (LD) and liquid ordered (LO) phases are represented in magenta and green, respectively. PEG molecules of PEGylated lipids are drawn in yellow and cholesterol is represented in light blue.

confocal microscopy. Due to the small size of the cubic particles, however, the acquisition of 3D stacks turned out to be challenging and we restricted the measurement to the equatorial plane. Finally, by fitting the experimental images and assigning a binary value to each pixel within the fitted surface (see Subsection 3.2.5), we measured the percentage of area occupied by the LD phase, which we denote as φ.

We found that the likelihood of configurations that are in the mixed state is affected by the geometry of the substrate. By collecting data for 200 CSLBs of each shape, we observed that 78% of the spheres were in the mixed state. This percentage decreased to 32% and 8% for symmetric and asymmetric dumbbells, respectively. Since all external conditions were kept identical, we infer that the geometry must promote the segregation of lipids. We note that our measurements are not dependent on the type of silica of the colloidal surface. On this note we report measurements of likelihood of phase separation on different silica surfaces in the Appendix, Figure A.2.

A simple way to organise our data for segregated CSLBs is to order them by their value of φ, *i.e.* by the percentage of their surface occupied by POPC-rich domains. Note that

this classification is inherently one-dimensional and is not directly linked with the relative amount of the three lipids on a single CSLB. The latter quantity would correspond to a point within the Gibbs phase triangle. Despite this last quantity would be more interesting to study than φ, unfortunately we do not have experimental access to it. The result of this procedure for the different geometries that we have considered is shown in Figure 3.5.

We observed a correlation between the underlying scaffold curvature and size, structure, and location of the phase domains. Since spheres are uniformly curved, domain equilibration dynamics is mainly driven by interface length minimisation, which systematically relaxes towards the formation of two domains bounded by a single interface (see Figure 3.5a). In contrast to previous experiments in which the membrane consisted of multiple coexisting domains (see *e.g.* Madwar *et al.*[74]), this observation suggests that our system has likely reached equilibrium already a few minutes after cooling.

Geometric effects emerge already for cubic CSLBs, where the principal curvatures of the surface are non-uniform and higher at corners and edges. From the equatorial sections of Figure 3.5b we see that, at low φ, LD domains are predominantly located alongside edges. We take this as a confirmation of the fact that softer domains tend to stick to regions of higher curvature[4;5;7;12;17;18;65;131] due to their lower bending cost. For higher φ we could not identify any geometric pinning, as the lack of a complete 3D reconstruction does not allow us to draw further conclusions. Still, 27% of 561 phase-separated cubes analysed showed three or more domains, indicating that the presence of curvature inhomogeneities is competing with the minimisation of the interfacial line tension, which hinders the coalescence of the lipid domains.

More dramatic curvature effects were seen in symmetric dumbbells, where interface location was almost always correlated to the underlying geometry, as shown in Figure 3.5c. For the phase-separated particles with low φ (below $\sim 23\%$) that we collected, the POPC-rich phase was pinned to the highly curved neck. However, the vast majority (87%) of dumbbells instead had $\varphi \sim 50\%$, with two different lipid compositions on each spherical lobe and an interface along the small neck-like region. Particles with higher φ value exhibited an interface lying along one of the lobes, somewhat resembling - on a single lobe - the configurations of Figure 3.5a. Interestingly, no particle was ever seen to lie in the range $24 - 50\%$. This gap in the percentage of area is shown as a dashed segment in Figure 3.5c.

Although with our methods we cannot assess the absolute amounts of lipids within a given phase, from the dumbbells of Figure 3.5c with $\varphi \sim 50\%$ we infer that there must be some mechanism keeping the interface at the neck, at the expense of changing the local composition of the membrane. Note that while variability in phase composition is a common feature of ternary systems - different points in the Gibbs phase diagram belong to different tie-lines - this effect alone cannot explain the different concentrations of dumbbell lobes. If it could, we would have observed the same phenomenon on spheres and cubes. Therefore, our results suggest that we observe the gap because of curvature. The lipid membrane adapts its tie-line in order to accommodate the interface in a specific location. While curvature-dependent lipid partitioning in GUVs has been seen before[6–8], for our dumbbell-shaped system we term the state observed in our

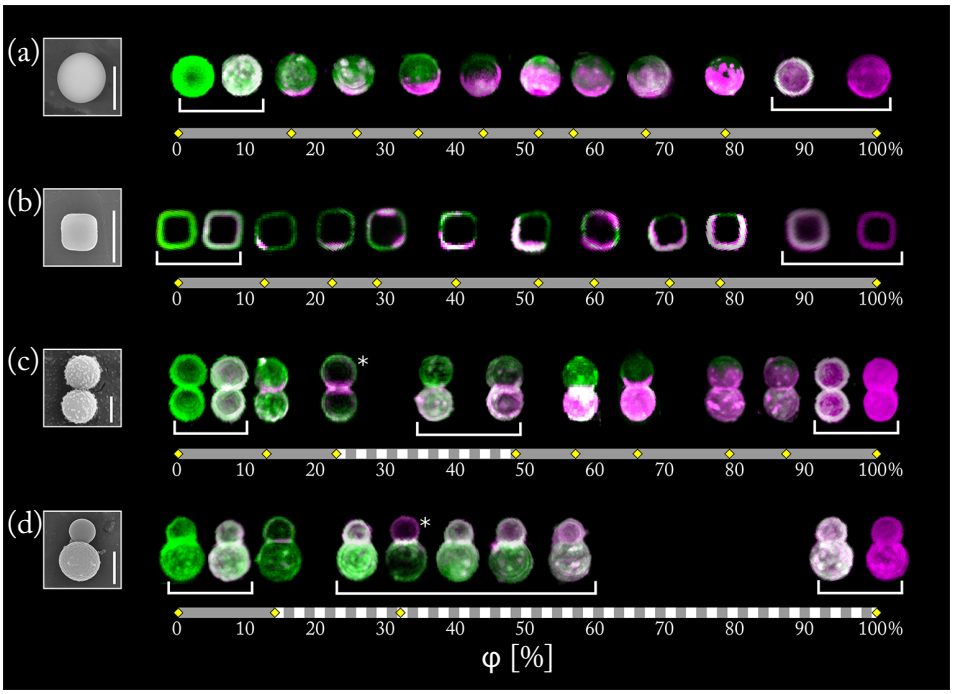

Figure 3.5: Representative collection of segregated CSLBs ordered by percentage of area occupied by the LD phase φ. The left panel shows scanning electron microscopy (SEM) images of **(a)** spherical, **(b)** cubic, **(c)** symmetric, and **(d)** asymmetric dumbbell-shaped particles. The right panel shows the corresponding CSLBs. For spheres and dumbbell-shaped particles, 3D reconstructions are reported. For cubic-shaped particles, equatorial sections are reported. For each of the four different shapes considered, we order the membrane configurations by the relative surface area occupied by the POPC-rich domains. Yellow rhombuses on the horizontal bars indicate measured values of φ. Dashed portions of the bar correspond to gaps, *i.e.*, ranges in the percentage of area occupied by the LD phase for which no configurations have been observed. Homogeneously mixed and antimixed configurations grouped with a white parenthesis correspond to the same value of φ and thus to a single rhombus. Antimixed configurations are configurations presenting concentrations of the sub-domains lying on opposite sides of a local miscibility gap. Experimentally, in Figure 3.7, we show that antimixed configurations present two coexisting domains of different chemical lipid compositions. In each of these domains, the lipids are perfectly mixed. See Table A.2 in the Appendix for the values of percentage of area occupied by the LD phase. The asterisks label the two configurations that will be used in the numerical simulations in Figure 3.8. Scale bars 2 μm.

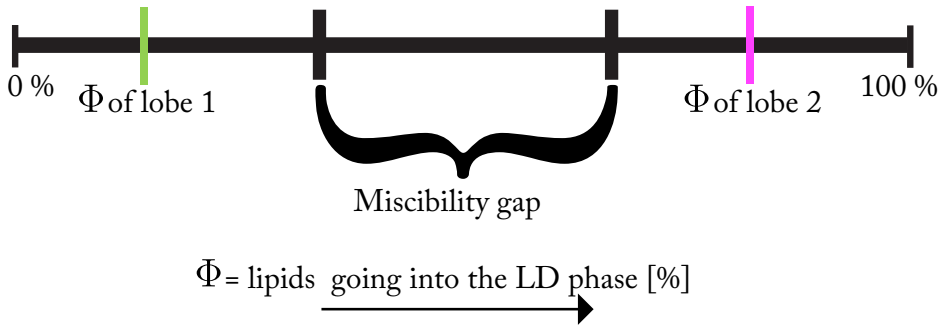

Figure 3.6: Schematic definition of antimixing. In the antimixed configurations, the percentages of lipids going into the LD phase of the single lobes $\{\Phi_1, \Phi_2\}$ are located on antipodes, *i.e* opposite sides, of the local miscibility gap. The notation $\{\Phi_1, \Phi_2\}$ will also be used in Section 3.5. We stress that it is different from $\{\varphi_1, \varphi_2\}$ which indicate the percentages of area occupied by the LD phase in the two lobes.

measurements antimixing because the concentrations of the sub-domains are located on antipodes, *i.e* opposite sides, of the miscibility gap. In Figure 3.6, we report a schematic definition of antimixing and in Section 3.5, we will show the theoretical analysis that is behind the formulation of our definition. We stress that antimixing is (1) a thermodynamic state, and not phase, (2) that it can be induced by any location-dependent coupling of the mixture concentration, and (3) that it becomes relevant only in closed systems.

The presence of gaps and antimixed configurations is further enhanced in the case of the asymmetric dumbbell-shaped particles (see Figure 3.5d), where there is an additional curvature asymmetry between the lobes of the dumbbell. Such phase-separated CSLBs exhibit three domains for $\varphi \lesssim 13\%$ with the LD phase located along the neck, and two coexisting domains above this value. In the latter case, the interface always lies along the neck and lobe compositions vary continuously, producing a gap that extends all the way to $\varphi = 100\%$. In Figure 3.7, we investigate this effect experimentally. The intensity of the two fluorescent channels normalised with their maximum intensity is measured along the long axis of the particle.

In a phase-separated state, the LO and LD phases produce intensity maxima on different regions of the membrane, as is the case in Figure 3.7a. In a mixed state (Figure 3.7d), the maxima overlap on both lobes indicating that the lipids are mixed on the whole surface. However, in an antimixed configuration, as in Figure 3.7b and c, the CSLBs exhibit same intensity maxima on the same lobe, while differing in the relative intensity on the other lobe. We will show later theoretically how this state differs from the classical mixed and phase-separated states, but we can already conclude experimentally that this state is a direct consequence of the stabilisation of the membrane on a closed substrate. The elastic coupling with curvature and the stability of the interface at the neck, already observed in previous works[4;17;66], induces a strong partitioning of the lipids in the two

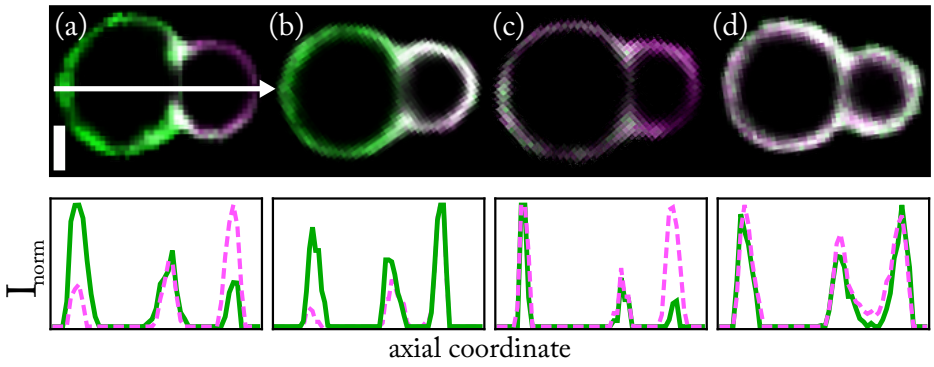

Figure 3.7: Experimental configurations. Equatorial plane images (**Top**) and intensity profiles (**Bottom**) for asymmetric dumbbell-shaped particles. The fluorescence intensity is sampled along the symmetry axis as shown by the white arrow in the top-left image, and normalised over the maximum of the channel. The green and magenta are represented with joined and dotted lines, respectively. The image shows four possible scenarios. In **(a)**, green and magenta peaks are on opposite lobes. In **b** and **(c)** the peaks are on the same lobe but the intensity is not uniform over the membrane. **(d)** shows a uniform membrane composition, where the two intensities are similar over the whole axis. Scale bar 2 μm.

lobes. We hypothesise that if the membrane would be allowed to change shape it would deform to accommodate the different lipid domains. In our system, however, this is not possible because the membrane is fixed on a substrate of specific geometry and therefore the lipid composition of the membrane in the two lobes must adjust according to the membrane geometry and total lipid composition.

Finally, we note that the percentages of particles in the mixed state reported previously (78%, 31%, and 8% for spheres, symmetric and asymmetric dumbbells, respectively) describe the mixed configurations such as the one in Figure 3.7d, and do not include the antimixed configurations.

In the next sections, we will first estimate the elastic parameters of the membrane by conducting a direct comparison between experiments and numerical simulations, and then we will show how curvature affects the free energy of the membrane and leads to the antimixed state.

3.4 Estimation of elastic parameters

We model the membrane as a closed two-dimensional surface S with different phases separated by a sharp interface L. Following the classical model of Jülicher and Lipowsky for multicomponent vesicles[63] based on the Cahnham-Helfrich energy[59;60], we associate to any domain configuration the free energy reported in the Introduction, Equation 1.15. Since the stiffer phase has higher bending rigidity k, we refer to the "+" and "-" domains as the portions of S occupied by the LO phase and LD phase, respectively. Since in our

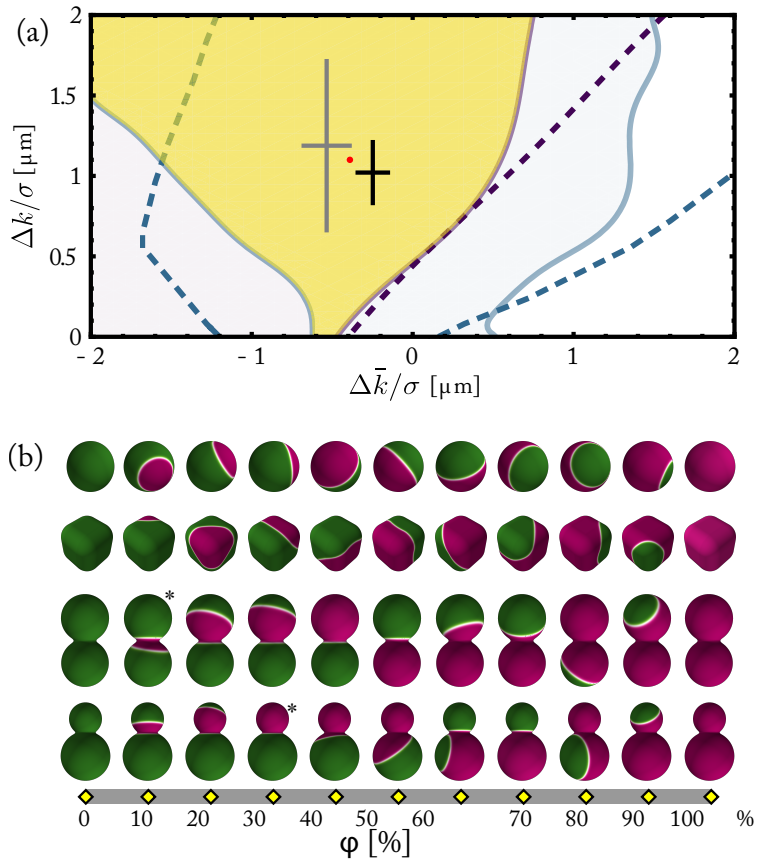

Figure 3.8: Elastic moduli differences and interface models. **(a)** In the two-dimensional parameter space spanned by $(\Delta k/\sigma, \Delta\bar{k}/\sigma)$, the yellow region shows the parameter values for which the minimal-energy configurations match with the experimental observations for the two CSLBs highlighted by the white asterisks in Figure 3.5. The solid lines correspond to the boundaries of allowed parameters for the symmetric (blue) and asymmetric dumbbell-shaped (violet) configurations obtained via minimisation of the diffuse interface model, Equation 3.4. The dashed lines show the analogous result obtained from minimising the sharp interface model Equation 3.3 under the further assumption of an axis-symmetric interface. For further comparison, we show measurements of these parameters obtained previously using GUVs. The points with error bars are from Baumgart *et al.*[65] (grey) and Semrau *et al.*[66] (black), and their average is shown by a red dot. **(b)** Theoretical diagrams of the percentage of area for the four geometries used in the experiments obtained by minimising the diffuse interface energy Equation 3.4 (green and magenta colours correspond to LO and LD phases, and white to the interfacial region). The asterisks depict the two configurations that match the ones highlighted in Figure 3.5. These models cannot reproduce the observed gaps. In the Appendix "Details on the numerical simulations of Chapter 3", we report details on the numerical simulations to obtain this figure.

set-up the shape of S is kept fixed, the only undetermined degrees of freedom are the position, shape, and topology of L. We further assume that, after coating, in any given CSLB there is no lipid exchange with the surrounding environment and thus the relative area fraction occupied by each phase is fixed. We enforce this constraint and the fact that the total surface area is not changing by means of two Lagrange multipliers $\lambda_{+,-}$.

Using tools from the classical theory of curves and surfaces, we compute functional variations of Equation 1.15 under the fixed φ constraint (the area fraction occupied by the "-" phase). The first variation leads to the force balance equilibrium condition:

$$\sigma\kappa_g = \Delta k\, H^2 + \Delta\bar{k}\, K + \Delta\lambda\,, \tag{3.3}$$

relating the interface's geodesic curvature κ_g and the interfacial line tension σ to the differences of bending moduli $\Delta k = k_+ - k_-$, saddle-splay moduli $\Delta\bar{k} = \bar{k}_+ - \bar{k}_-$, and Lagrange multipliers $\Delta\lambda = \lambda_+ - \lambda_-$ between the two phases. The mean (H) and Gaussian (K) curvatures on the right-hand side are evaluated on S. Definition of the curvatures can be found in Chapter 1, Section 1.4.1. Note that solutions of this equation depend effectively on only two physical parameters: $\Delta k/\sigma$ and $\Delta\bar{k}/\sigma$, as $\Delta\lambda$ can be arbitrarily changed in order to enforce the desired φ value. Both these quantities have dimension of length and their values are typically in the micrometre range.

Equation 3.3 can be considered as the two-dimensional analogue of the Young-Laplace equation for liquid-liquid interfaces: on a flat substrate, where both H and K vanish, its solutions describe a circular droplet of radius $\sigma/\Delta\lambda$, with the Lagrange multipliers effectively working as a pressure differential across the interface. For spherical particles of radius R, for which $H^2 = K = 1/R^2$, the equilibrium interface lies along constant geodesic curvature lines, *i.e* circles, whose total area is fixed solely by the value of φ. Furthermore, a single, non-maximal circle is the most stable interface, which is consistent with Figure 3.5a and the fact that we never observed more than two domains on spherical CSLBs.

More general surfaces usually have non-constant H and/or K, in which case the interface equation becomes significantly more difficult to solve, even with numerical tools. This happens because Equation 3.3 is only a local relation, while the interface is subject also to global constraints, since L must be embedded, closed and must minimise Equation 1.15 among all possible topologies. Some specific cases are nonetheless more tractable, such as axisymmetric surfaces and interfaces. Note however that while it seems reasonable to assume that our dumbbells are rotationally symmetric, it is not necessarily obvious that interfaces on them will inherit this symmetry.

To overcome this computational difficulty we employ a diffuse interface model[142;143], where the line L is replaced by the steep variation of a space-dependent scalar field ϕ. The equilibrium configurations of ϕ are determined by minima of a Ginzburg-Landau type of free energy

$$F = \int_S \mathrm{d}A\, \left[\frac{\epsilon}{2}|\nabla\phi|^2 + \frac{1}{\epsilon}f(\phi) + k(\phi)H^2 + \bar{k}(\phi)K\right]\,. \tag{3.4}$$

While the gradient term in the energy favours gently-varying field configurations, the second term, $f(\phi) = f_0\phi^2(\phi-1)^2$, is a double-well potential that favours phase-separated

configurations, where ϕ is constant over portions of S which we identify as the LD (with $\phi = 0$) and LO (with $\phi = 1$) domains. The parameter ϵ controls the thickness of the interfaces separating the two phases. In the thin interface limit, $\epsilon \to 0$, the first two terms of Equation 3.4 converge to the second term of Equation 1.15 with line tension $\sigma = \frac{2}{3}\sqrt{2f_0}$. The functions $k(\phi)$ and $\bar{k}(\phi)$ represent the elastic moduli of the LO and LD phases and can be parametrised as $k(\phi) = \Delta k\, g(\phi)$ and $\bar{k}(\phi) = \Delta\bar{k}\, g(\phi)$, with Δk and $\Delta\bar{k}$ the same as in Equation 3.3 and $g(\phi)$ a dimensionless function interpolating between 0 and 1. Here we choose $g(\phi) = \phi^2(3 - 2\phi)$, but the precise form of this function is unimportant in the $\epsilon \to 0$ limit. Finally, mass conservation is enforced via a single Lagrange multiplier λ, so that the total energy is given by $F + \lambda \int_S \mathrm{d}A\, \phi$. Equilibrium configurations are found via a non-local gradient descent of Equation 3.4.

We have employed both the axis-symmetric sharp interface and the diffuse interface models to estimate the values of $\Delta k/\sigma$ and $\Delta\bar{k}/\sigma$ for CSLBs, as shown in Figure 3.8a. To qualitatively compare our models with experiments, the colloidal shape was extracted from SEM images and we estimate an area of 44.6 μm^2 for the symmetric dumbbell and 28.4 μm^2 for the asymmetric dumbbell-shaped particles. Then, using either of the two models, we checked for which parameter values we could reproduce the neck-pinned LD domain for the dumbbell at $\varphi \sim 10 - 20\%$ and the smaller-lobe-pinned LD domain at $\varphi \sim 30\%$ for the asymmetric dumbbell. We labelled these two configurations with a white asterisk in Figure 3.5c and d.

The yellow region in Figure 3.8a shows the parameter values where numerical results match experimental observations. We found that the two models produce qualitatively similar but not identical results. We ascribe the difference to the different assumptions on the symmetry of the interface.

Interestingly, we found agreement for the material parameters with previous measurements obtained from free-standing vesicles[65;66]. We are not able to reach the same accuracy of these works, because our CSLBs are roughly one order of magnitude smaller in size than GUVs and we cannot optically resolve the precise shape of the neck regions. Furthermore, the scaffold makes our system less sensitive to large values of $\Delta k/\sigma$ and $\Delta\bar{k}/\sigma$ since bending-induced out-of-plane stresses - which would create major shape changes in GUVs[143;144] - are adsorbed by the rigid structure of the underlying colloids. The consequence of this is that, with CSLBs, we cannot expect to get absolute upper bounds on the model parameters.

One could further expect it would be possible to estimate the membrane's elastic parameters with higher precision by including further experimental images, either from additional geometries or φ values, leading to a smaller yellow region in the phase diagram. This is however not possible because the sharp interface theory is inherently unable to explain the observed variability in the composition and the gaps of Figure 3.5c and d. In fact, by using parameters value compatible with our and previous estimations (specifically, $\Delta k/\sigma$ = 1.10 μm and $\Delta\bar{k}/\sigma$ = -0.39 μm, shown as a red dot in Figure 3.8a), we reconstructed the theoretical diagrams for the percentage of area occupied by the LD phase in Figure 3.8b. While for spherical CSLBs the model correctly predicts the coexistence of two domains and a single interface, in agreement with Figure 3.5a, for dumbbell-shaped

CSLBs it fails completely. In particular, for the asymmetric dumbbell-shaped particle, we should have observed for $\varphi \gtrsim 30\%$ interfaces positioned away from the dumbbell's neck.

The reason behind this discrepancy lies in the fact that the non-trivial curvature of the CSLBs directly influences the lipid sorting rather than just inducing geometric effects on domain displacement. Since the model of Equation 1.15 can account only for the latter, it is deemed to have little explanatory power when confronted with our experiments. In the next section, we will explain how to explain our observations.

3.5 Curvature-composition interactions

Our experiments show a correlation between shape and local chemical composition of dumbbell-shaped CSLBs: lipids tend to cover uniformly the spherical lobes leaving the interfacial region along the neck, with the POPC molecules clearly preferring lobes of higher curvature. The large variability of relative concentrations (see Figure 3.5c and d) implies that it is energetically favourable to have a chemically homogeneous membrane over a single lobe rather than accommodate an interface away from the neck. As explained earlier, this phenomenon cannot be described only by the random spread of CSLBs along different tie-lines. We infer that it is the bilayer shape that influences the thermodynamic equilibria of the lipid mixture.

A consistent model incorporating such effects must allow for situations where the membrane lipid content is directly coupled to geometrical features. In Chapter 4, we will review previous works on the subject and outline the general principles behind the construction of such models. In the following, we will explain how this approach can explain the observed gaps present in the experimental diagram in the simpler and more tractable case of a binary mixture, *i.e.* a membrane consisting of only two different types of molecules. Therefore, the following discussion is to be intended as a qualitative explanation of the underlying phenomena in CSLBs, keeping in mind that a quantitative understanding is possible only when considering ternary systems.

A thermodynamically closed system consisting of two incompressible species can be described by a single scalar order parameter, which we denote again by ϕ. Note however its conceptual meaning is now different: whereas ϕ in Equation 3.4 is a mathematical parameter whose value sets L, now it stand for the physical concentration of one of the two molecules at any point on the membrane surface. As such, we associate the extreme values $\phi = 0, 1$ to membrane portions consisting exclusively of one of the two molecules. Since thermodynamically stable phases are never pure, the concentrations corresponding to the LO and LD phases will strictly lie within the interval $0 < \phi < 1$.

The Helmholtz free energy of the binary system can then be written as

$$F = \int_S \mathrm{d}A \left[\frac{D}{2} |\nabla \phi|^2 + f(\phi) + k(\phi) H^2 + \bar{k}(\phi) K \right] . \tag{3.5}$$

This expression, although formally similar to Equation 3.4, carries a very different meaning, since now it can be used to assess the thermodynamic stability of mixed versus demixed phases. The homogeneous part of the free energy density is $f(\phi) = u(\phi) - Ts(\phi)$, with $u(\phi)$ the internal energy and $s(\phi)$ the entropy densities. The area compressibility

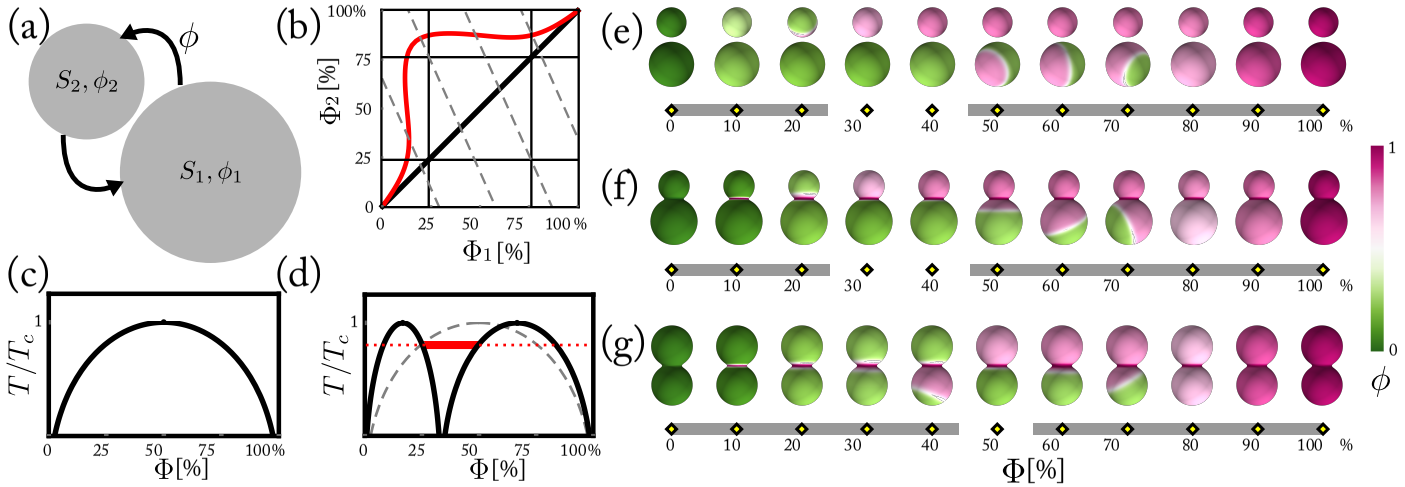

Figure 3.9: The antimixed state. (a) Schematic representation of the two-spheres approximation of the asymmetric-dumbbell-shaped particle of Figure 3.5d. **(b)** Equilibrium lines in the absence (black) and presence (red) of curvature coupling L_k in the energy Equation 3.5. The vertical and horizontal background lines correspond to the binodal concentrations on each sphere. Dashed oblique lines correspond to fixed values of $\Phi.\Phi_1$ and Φ_2 are the total concentrations relative to the larger and smaller sphere, respectively. **(c)** Composition-temperature phase diagram for the classical lattice-gas binary mixture, with a binodal line culminating at the critical point at $\Phi = 50\%$. **(d)** Composition-temperature phase diagram for the two-sphere system when $L_k = 0.14 T_c R_1^2$, with R_1 the radius of the largest sphere. The binodal line of the classical picture (dashed grey) splits into two lines which determines sub-diagrams where phase separation occurs on either one of the two spheres. The red line corresponds to $T = 0.9 T_c$, used in the numerical simulations. The thicker red segment locates the range of the antimixed state for that temperature. **(e)** Numerically found concentration diagrams of the two spheres at $T = 0.9 T_c$. Note that at $\Phi = 0, 100\%$ also $\varphi = 0, 100\%$, but otherwise the two values do differ. For $\Phi \sim 30 - 40\%$ (white bar) we indeed observe antimixed states. **(f-g)** Numerically found concentration diagrams for the connected symmetric and asymmetric dumbbell-shaped geometries. In this case both antimixed states and the geometric pinning along the neck are observed. In the Appendix "Details on the numerical simulations of Chapter 3", we report details on the numerical simulations to obtain this figure.

coefficient D is taken to be infinitesimal and to scale as $\sim \epsilon^2$ where now ϵ is the physical thickness of the interface. Notice that differently from Equation 3.4, the concentration-dependent curvature couplings enter at the same order as $f(\phi)$, *i.e.* $k(\phi)$ and $\bar{k}(\phi)$ contribute directly to the thermodynamic stability, rather than just affecting interfacial position. Inspired by the canonical mean-field continuum approximation of the 2D lattice-gas model, here we take $u(\phi) = J\phi(1-\phi)$, $s(\phi) = -k_B[\phi\log\phi + (1-\phi)\log(1-\phi)]$, $k(\phi) = L_k\phi$ and $\bar{k}(\phi) = L_{\bar{k}}\phi$.

We can now minimise Equation 3.5 for all experimental geometries with the constraint of keeping the total concentration $\Phi = \frac{1}{A}\int \mathrm{d}A\,\phi$ fixed. Note that in these settings, Φ approximately equates φ only for phase-separated states. To obtain a semi-analytical understanding of the gaps, we first considered a simplified geometry where asymmetric dumbbell-shaped particles are approximated by two disjoint spheres of radii $R_1 > R_2$, allowed to exchange molecules among each other (see Figure 3.9a). For this particular system it is possible to formulate the problem in terms of the two average concentrations ϕ_i on each sphere. By varying the total Φ, a series of points in the $\{\Phi_1, \Phi_2\}$ plane can be obtained, as we show in Figure 3.9b. These determine the equilibrium state reached by the whole system. In absence of curvature coupling (black line in Figure 3.9b), the trivial mixed state $\Phi_1 = \Phi_2$ is reached, *i.e.* a situation where the membrane is entirely uniform. Instead if $L_k \neq 0$, the energetic cost of having $\phi \neq 0$ on a sphere depends on its diameter, leading to a displacement of the equilibrium line (red line in Figure 3.9b). It is possible to prove that these states are stable against phase separation, and thus are, for certain values of Φ, true minima of the free energy and that they are continuously connected to the usual mixed state at higher temperature. We note that these states that lie on the red line in Figure 3.9b were previously shown in the one-dimensional schematic representation in Figure 3.6.

This phenomenon becomes more intuitive when considering the concentration and temperature phase diagram of the mixture. The classical case of the lattice-gas model with conserved order parameter is shown in Figure 3.9c: there is one critical point, and for Φ and T values that lie above the binodal line (shown as a thick black line), homogeneous mixing is the thermodynamic equilibrium. When switching on the coupling with curvature, the binodal splits into multiple sub-lines with a local critical point for each sphere, see Figure 3.9d. The region above the binodals still corresponds to mixed states which, however, become non-homogeneous for sub-critical temperatures. The region containing the thick red line in the diagram is where antimixed states are stable because they are absolute minima of the free energy.

In Figure 3.9e, we show the concentration diagram, at $T = 0.9T_c$, of the two spheres, corresponding to the red dotted line in Figure 3.9d. Note that now, differently from Figure 3.8, the colour intensity of different domains can change continuously and is neither pure green (corresponding to $\phi = 0$) nor pure magenta ($\phi = 1$), as shown in the legend on the right. We find that the antimixed state happens for $\Phi \sim 30 - 40\%$, with equilibrium configurations that are reminiscent of Figure 3.5d. Interestingly, the antimixed state continues to be valid even for more realistic shapes: in Figure 3.9f, we show the analogous concentration diagrams for the asymmetric dumbbell-shaped geometry, in

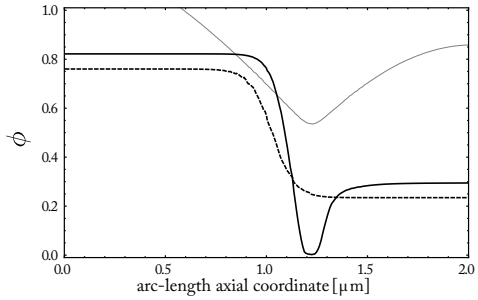

Figure 3.10: Comparison of interfacial profiles. Local concentration ϕ as a function of the arc-length axial coordinate for the asymmetric dumbbell-shaped particle at $\Phi = 35\%$. The solid and dashed lines correspond respectively to the antimixed state (see Figure 3.9f) and to standard phase separation (see Figure 3.8b). The profiles have been obtained numerically by minimising respectively Equation 3.4 and Equation 3.5. While the standard phase-separated state is the typical monotonic kink-like curve interpolating between two binodal concentrations, in the case of antimixing - even with linear coupling - the curve is not monotonic and interpolates between average concentrations on the spheres that are precisely the ones predicted by the two-spheres model of Figure 3.9a-e. The thin grey curve in the background shows, for reference, the shape profile of the asymmetric dumbbell-shaped geometry.

which Equation 3.5 is minimised on this connected geometry. The average concentration at the lobes follows the same equilibrium line of Figure 3.9b, and thus for approximately the same values of Φ as for the two-spheres, the equilibrium state is antimixed. This is shown by the interface profiles of Figure 3.10: the antimixed state (solid black line) interpolates between non-binodal values in the two lobes, and does so in a non-monotonic fashion. This situation is very different from the standard phase separation - used *e.g.* in Figure 3.8b - where the concentration at the interface follows a hyperbolic tangent curve (dashed black line). For lower Φ values there are geometrically pinned domains, similar to both the prediction of the sharp interface model (Figure 3.8b) and to the experimental ones (Figure 3.5d). Furthermore, at high Φ values the two lobes are both in an almost-homogeneous mixed state, where the intensity of magenta on the two lobes is slightly different: this is similar to to the curvature-induced lipid sorting observed in membrane tubes[6–8], with the only difference being that in our case all geometrical features are of similar size. Finally, Figure 3.9g shows the same concentration diagram for the symmetric dumbbell, with similar interpretations. Again, it can be proved that the average concentration of the two lobes at $\Phi = 50\%$ does not match the binodal values and as such it corresponds to an antimixed state.

3.6 Conclusions

In this chapter, we have used for the first time colloid supported lipid bilayers (CSLBs) to decipher the complex physics of phase separation on curved surfaces. The colloidal

scaffold imposes its geometry onto the supported lipid membrane allowing an independent study of geometry-induced effects on closed membranes. It is well-known that the LO and LD phases posses different elastic properties and react differently to bending, which induces the geometric pinning of softer LD domains in regions of higher curvature [4;5;18]. We observed this effect in CSLBs, which allowed us to estimate the LO/LD elastic moduli differences, finding compatible results with previous measures from Giant Unilamellar Vesicles (GUVs) experiments [65;66]. We found, however, that the standard sharp interface model employed for such estimates [63] was not adequate to explain the full phenomenology of CSLBs; in fact, the unique combination of closeness and fixed geometry gives rise to a new phenomenon, which we termed antimixing, where lipids segregate in a state which is continuously connected to a purely mixed phase. This phenomenon is similar in nature to the predicted behaviour of multicomponent lipid membranes on patterned adhesion substrates [126]. In our case the source of inhomogeneity is provided by curvature, and it is similar to curvature-driven sorting [6–8]. In our case, the membrane has sub-domains located on antipodes of the miscibility gap.

While the interplay between geometry and domain localisation has been previously observed [4;5;7;12;17;18;65;131], setting both the shape and the composition of the membrane allowed us to deepen our understanding of the delicate balance between membrane curvature and composition. Although we can qualitatively explain every aspect of our findings, it is evident that a fully quantitative description is still missing. This is due to the fact that our system is ternary, and a general understanding of the energy landscape of three-component systems is still lacking. Such a model, because of geometry-dependent tie-lines and interface compositions, could explain the full extent of the gaps in the experimental diagrams of the percentage of area.

Our results can be extended to other two-dimensional physical systems exhibiting phase separation [145]. Furthermore, the membrane-coated colloids developed here can switch their surface properties and interactions [55] from uniform to site-specific, paving the way for smart materials and biomedical applications such as sensing, imaging and drug delivery. To achieve this goal, control of the lipid composition on single CSLBs would be highly useful and could be achieved by depositing lipids on the colloids with micro-fluidic techniques analogous to studies with emulsions [146].

Acknowledgements

I thank Piermarco Fonda, who has done the theory and the simulations and co-wrote the paper with me. Furthermore, I would like to thank Rachel Doherty and Vera Meester for help with the colloidal syntheses and electron microscopy imaging.